coatings

MDPI

Article

First Principles Calculation of the Influence of Alloying on the Phase Stability, Elasticity, and Thermodynamic Properties of the MoNbTiVX (X = Al/Cr) Refractory High-Entropy Alloy

Lin Chen [1,2,3,†], Weijun Li [2,3,†], Weihe Shi [2,3], Liuqing Liang [2,3], Jinghui Sun [2,3], Chengchu Yin [4], Jiafei Yi [2,3], Xuming Zhang [2,3], Peilin Qing [2,3], Alin Cao [2,3], Xiaowei Zhang [1,*] and Hongxi Liu [1,*]

1 Faculty of Materials Science and Engineering, Kunming University of Science and Technology, Kunming 650093, China; linchen_chn@vip.126.com
2 Guangxi Key Laboratory of Green Manufacturing for Ecological Aluminum Industry, Baise University, Baise 533000, China; liweijun_bsu@163.com (W.L.); shiweihe@bsuc.cn (W.S.); 02xbllq@163.com (L.L.); sjh270349234@bsuc.edu.cn (J.S.); yijiafei@bsuc.edu.cn (J.Y.); zhangxuming3000@bsuc.edu.cn (X.Z.); plqing110@163.com (P.Q.); caoalin@163.com (A.C.)
3 Engineering Research Center of Advanced Aluminium Matrix Materials of Guangxi Province, Baise University, Baise 533000, China
4 Guangxi Zhongke Petrochemical Research Institute Testing Co., Ltd., Nanning 530105, China; 15977149047@163.com
* Correspondence: zhxw72@163.com (X.Z.); piiiliuhx@sina.com (H.L.)
† These authors contributed equally to this work.

Abstract: In response to the poor wear resistance and high-temperature oxidation resistance of titanium alloys during service, a series of lightweight refractory high-entropy alloys (RHEAs) can be designed for the laser cladding coating of titanium alloy surfaces, with due consideration of the compositional and structural characteristics of titanium alloys. Firstly, the structural stability, mechanical and thermal properties of four lightweight RHEAs (MoNbTiV, AlMoNbTiW, CrMoNbTiV, and AlCrMoNbTiV) with equal atomic ratios were designed and calculated using first principles combined with quasi-harmonic approximation (QHA). The results indicate that all four RHEAs are stable BCC, exhibiting elastic anisotropy and ductility. The lightest density is 6.409 g/cm^3. Adding Al/Cr can cause structural distortion and affect its mechanical properties. Their Young's moduli are in the following order: AlCrMoNbTiV > MoNbTiV > CrMoNbTiV > AlMoNbTiV. The thermal expansion coefficients of the four RHEAs and titanium alloys are very close, with a difference in linear expansion coefficient of less than 1.16 × 10^{-5}/K. Meanwhile, the metallurgical bonding of four types of RHEA coatings was successfully achieved on a Ti-6Al-4V(TC4) substrate through laser cladding technology, and all coatings exhibited a unique BCC solid solution phase.

Keywords: high-entropy alloy; first principles; elasticity; coating; laser cladding

check for updates

Citation: Chen, L.; Li, W.; Shi, W.; Liang, L.; Sun, J.; Yin, C.; Yi, J.; Zhang, X.; Qing, P.; Cao, A.; et al. First Principles Calculation of the Influence of Alloying on the Phase Stability, Elasticity, and Thermodynamic Properties of the MoNbTiVX (X = Al/Cr) Refractory High-Entropy Alloy. *Coatings* **2024**, *14*, 1399. https://doi.org/10.3390/coatings14111399

Academic Editor: Rafael Comesaña

Received: 24 September 2024
Revised: 27 October 2024
Accepted: 1 November 2024
Published: 4 November 2024

Copyright: © 2024 by the authors. Licensee MDPI, Basel, Switzerland. This article is an open access article distributed under the terms and conditions of the Creative Commons Attribution (CC BY) license (https://creativecommons.org/licenses/by/4.0/).

1. Introduction

Titanium and its alloys have many excellent properties, such as high specific strength, low density (about 4.5 g/cm^3), resistance to atmospheric corrosion, and good resistance to high and low temperatures. Therefore, they are widely used in the aerospace field. With the rapid development of aerospace industry technology, titanium alloy components usually need to be used in high-temperature environments. However, their application is severely restricted due to the titanium alloys' poor wear and high-temperature oxidation resistance [1,2]. Wear and oxidation resistance are characteristics related to the surface of materials, and the failure of titanium alloy parts mostly starts from the surface or its surface layer. In response to these shortcomings, some surface modification methods, such as thermal spraying [3], plasma-based ion implantation (PBII) [4], plasma nitriding [5],

physical vapor deposition (PVD) [6], micro-arc oxidation (MAO) [7], chemical vapor deposition (CVD) [8], and electrochemical deposition (ED) [9], have been used to prepare coatings on titanium alloy parts to improve their wear resistance, oxidation resistance, and corrosion resistance. However, coatings prepared by the above methods typically have a thin thickness (<100 μm) [6–9], poor microstructure density [3–5], and low bonding strength with titanium alloy substrates [3–9]. In addition, due to the severe cracking and debonding sensitivity of titanium alloys, these methods cannot provide long-term high-wear resistance and high-temperature oxidation resistance to the surface of titanium alloys [10].

Laser cladding (LC) can achieve good metallurgical bonding between coatings and substrates [11]. The LC coating has good tissue density, and the coating thickness can be adjusted in the range of micrometers to millimeters while retaining the overall mechanical properties of the substrate material, thus obtaining an LC coating with excellent performance [12]. The preparation of particle-reinforced composite coatings by LC, such as titanium-based composite coatings [13], cobalt-based composite coatings [14], nickel-based composite coatings [15], and some composite matrix coatings [16], have been used to improve the wear resistance and high-temperature resistance of titanium alloys. However, new challenges have been discovered, such as high crack sensitivity and poor processing performance, which are the two inherent defects of such composite coatings.

The concept of high-entropy alloys (HEAs) has provided a new strategy to address the issues above [17]. HEAs are mainly composed of a single solid solution phase and do not contain complex intermetallic compounds, which can reduce cracking sensitivity, improve processing performance, and not cause severe damage to wear and high-temperature oxidation resistance [18]. Compared to other alloys, refractory high-entropy alloys (RHEAs) exhibit superior wear resistance, high-temperature mechanical properties, and high-temperature oxidation resistance [19,20]. Huang et al. [12] investigated the oxidation, thermal stability, and dry sliding wear behavior of AlCrSiTiV HEA coatings obtained by LC on Ti-6Al-4V substrates. Li et al. [21] deposited non-equiatomic AlBxCoCrNiTi (x = 0, 0.5, 1) high-entropy alloy coatings on the surface of a TC4 titanium alloy using LC and studied the microstructure, hardness, and wear resistance of HEA coatings. Wu et al. [22] a successful AlCoCrFeNiTi0.5 HEA coating was deposited on the surface of the TC4 substrate by LC deposition, which was metallurgical and bonded with the substrate. Cai et al. [23–25] used a premixed powder method to laser clad Ni-Cr-Co-Ti-V [23], Ni-Cr-Co-Ti-V-Al [24], and Ni-Cr-Co-Ti-V-Al [25] high-entropy alloy coatings on the surface of a TC4 alloy. Xiang et al. [26] successfully prepared CoCrFeNiNbx (x = 0 or 1 at.%) HEA coatings with good metallurgical bonding on the surface of pure titanium plates using a pulsed laser. The high-entropy alloy coatings obtained by these methods have varying degrees of improvement in hardness, wear resistance, and high-temperature oxidation resistance compared to titanium alloy substrates [12,21–26].

High specific strength and low density are the advantages of titanium alloys as the primary structural materials for aerospace. Therefore, it is necessary to design low-density RHEAs suitable for the LC process on the surface of titanium alloys, which have the excellent wear resistance and high-temperature oxidation resistance components of RHEAs. The MoNbTaW prepared by Senkov et al. [19,27] has attracted widespread attention due to its ability to maintain a high strength of about 590–600 MPa at 1600 °C. However, its higher-than-expected density (13.75 g/cm^3) and lower-than-expected room temperature ductility still need to be addressed. Replacing W with V in MoNbTaW, as the cast MoNbTaV alloy has a single BCC structure, with a high yield stress of ~1.5 GPa and a significant compressive fracture strain of ~21% at room temperature, which are both significantly higher than the MoNbTaW alloy [18], reduces its theoretical density to about 10.69 g/cm^3. Further, by replacing expensive and refractory Ta with Ti, the MoNbTiV alloy with an equal atomic ratio was obtained. At room temperature, its cast compressive yield strength reached 1200 MPa, compressive fracture strain reached 25.62%, hardness reached 440.7 HV, and theoretical density further decreased to 7.32 g/cm^3 [28].

Xiao et al. [29] combined first principles calculations with the quasi-harmonic approximation (QHA) model to investigate the relative energy stability, mechanical properties, and thermodynamic behavior of the B2-AlRE (RE = Sc, Y, La-Lu) secondary phase in aluminum alloys. Wang et al. [30] used first principles calculations to study the phase stability, thermophysical, and mechanical properties of refractory high-entropy alloys (RHEAs) at finite temperatures. Wang et al. [31] employed first principles calculations in conjunction with the quasi-harmonic approximation to effectively explore the mechanical, electronic, and thermodynamic properties of Mg-Al-Mn ternary compounds. These studies [29–31] have achieved promising results in different alloy systems, demonstrating the scientific feasibility of using a combination of first principles calculations and the quasi-harmonic approximation (QHA) model for the design of new alloy systems.

Based on the above references, the first principles design was adopted to develop MoNbTiVX (X = Al/Cr) RHEAs with good comprehensive performance and low density, providing a reference for the subsequent preparation of RHEA coatings on TC4 alloys using the LC technology to improve its wear resistance and high-temperature oxidation resistance. The addition of Al is to enhance the strength of the coating, as it has a high solubility in refractory metals and strong adhesion with them [20]. Similarly, Al with atomic radii similar to Ti and Nb also promotes the formation of solid solutions in the coating, and adding Al can significantly reduce the density of the alloy. However, the solid solution formed in MoNbTiV systems with similar atomic radii may exhibit lower hardness due to weak solid solution strengthening, which has a limited effect on improving the wear resistance of coatings. Considering this, Cr with significantly different atomic radii from Al, Mo, Nb, Ti, and V was chosen to improve the wear resistance of the coating, as it has a significant solid solution strengthening effect. In addition, as another refractory alloy element, Cr also helps to further improve high-temperature oxidation resistance [28,32]. Therefore, this article investigates the effects of the addition of Al and Cr on the phase structure, elasticity, and thermodynamic properties of RHEA coatings through first principles calculations to determine the optimal composition combination of RHEA coatings, providing valuable and cost-effective references for the surface modification of titanium alloys and engineering applications of RHEAs.

2. Details of Calculation Methods

2.1. Alloy Composition Design

To obtain the single-phase RHEA structure, the theoretical values of the thermodynamic parameters of the alloy composition need to meet specific criteria, as listed in Table 1.

Table 1. Thermodynamic empirical parameter formula and value range of high-entropy alloy [33–37].

Parameter	Calculating Expressions	Value Range	Ref.
Mixed entropy (ΔS_{mix})	$\Delta S_{mix} = -R\sum_{i=1}^{n} c_i \ln c_i$	$\Delta S_{mix} > 1.5R,\ R = 1.38 \times 10^{13} J/K$	[33]
Mixed enthalpy (ΔH_{mix})	$\Delta H_{mix} = \sum_{i,j=1,i\neq j}^{n} 4H_{mix}^{AB} c_i c_j$	$-20 \leq \Delta H_{mix} \leq 5 kJ/mol$	[34]
Atomic radius difference (δ)	$\delta = 100 \times \sqrt{\sum_{i=1}^{n} c_i \left(1 - \frac{r_i}{\overline{r}}\right)^2}$	$\delta \leq 6.6\%$	[35]
Composite parameter (Ω)	$\Omega = \frac{T_m \Delta S_{mix}}{\lvert \Delta H_{mix} \rvert}$	$\Omega \geq 1.1, \delta \leq 6.6\%$	[35]
Valence electron concentration (VEC)	$VEC = \sum_{i=1}^{N} c_i (VEC)_i$	$VEC < 6.87 \rightarrow BCC$; $VEC \geq 8.0 \rightarrow FCC$ $6.87 \leq VEC < 8 \rightarrow FCC + BCC$	[36]
Poor electronegativity ($\Delta\chi$)	$\Delta\chi = \sqrt{\sum_{i=1}^{n} c_i (\chi_i - \overline{\chi})^2}$ $\overline{\chi} = \sum_{i=1}^{n} c_i \chi_i$	$\Delta\chi < 0.117$	[37]

Note: for the meanings of other symbols in the table, please refer to Table S1 in the Supplementary Materials.

Design MoNbTiV, AlMoNbTiV, CrMoNbTiV, and AlCrMoNbTiV RHEAs (in the following text, these four alloys are represented as RHEA−1, RHEA−2, RHEA−3, and RHEA−4, respectively) with equal atomic ratios using pure metal elements of Al, Cr, Mo, Nb, Ti, and V. Theoretical density of RHEA system ρ. The calculation method for either refers to Equation (1) [19]. Where A_i and c_i are the atomic weights and densities of element i. The theoretical calculation values of thermodynamic parameters for the four RHEAs are listed in Table 2.

$$\rho_{\text{theor}} = \frac{\sum_{i=1}^{n} c_i A_i}{\sum_{i=1}^{n} \frac{c_i A_i}{\rho_i}} \quad (1)$$

Table 2. Values of thermodynamic parameters ΔS_{mix} (J/mol·K^{-1}), ΔH_{mix} (kJ/mol), δ (%), $\Delta\chi$, *VEC*, T_{m} (K), Ω, and theoretical density ρ_{theor} (g/cm^3) of RHEAs.

RHEAs	ΔS_{mix}	ΔH_{mix}	δ	$\Delta\chi$	*VEC*	T_{m}	Ω	ρ_{theor}
RHEA−1	11.53	−2.75	4.07	0.249	5.0	2442.5	10.24	7.358
RHEA−2	13.38	−12.80	3.80	0.228	4.6	2140.6	2.24	6.409
RHEA−3	13.38	−4.32	5.62	0.225	5.2	2390.0	7.40	7.331
RHEA−4	14.90	−11.78	5.41	0.209	4.8	2147.2	2.72	6.510

2.2. Model Construction and Elastic Modulus Calculation

The CASTEP (Cambridge Sequential Total Energy Package) code [38] calculates the full tensor of the second-order elastic constant and related mechanical properties, such as Poisson's ratio, Lamé constants, Bulk modulus, etc. Researchers can use computer simulations to conduct virtual experiments in these areas, significantly saving on expensive experiments and shortening development cycles. Special quasirandom structures (SQSs) [39] are an advantageous modeling method for periodic structure models given a random alloy. So far, the SQS method has been successfully applied to predict the formation energy, elastic properties, bond length distribution, density of states, bandgap, and optical properties of a series of materials with displacement disorder, including semiconductors, oxides, and metal alloys including HEAs [40]. The simplified SQS modeling thinking developed in recent years can achieve automatic model generation through the "mcsqs" code in the Alloy Theoretical Automated Toolkit (ATAT) [41,42]. The SQS crystal structure supercell model of RHEAs is processed using open-source VESTA software code for image processing [43]. Figure 1 shows the steel ball model diagram before the structural relaxation treatment of the SQS supercell model.

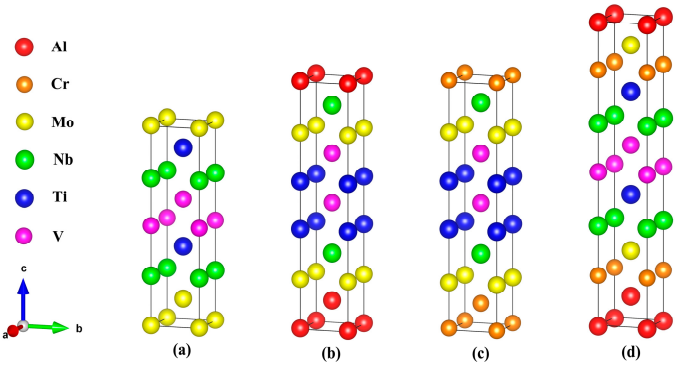

Figure 1. SQS supercell model of RHEAs before structural relaxation. (**a**) RHEA−1 1 × 1 × 4; (**b**) RHEA−2 1 × 1 × 5; (**c**) RHEA−3 1 × 1 × 5; (**d**) RHEA−4 1 × 1 × 6.

First principles calculations were performed using the CASTEP software, with the selected cut-off energy and k-point values fixed at 420 eV and 12 × 12 × 6, respectively. A series of energy–volume data pairs, totaling 30 sets, were generated and found to conform to

the Birch–Murnaghan isothermal equation of state (EOS), as described in Equation (2) [44]. These data points are depicted as blue circular markers in Figure 2.

$$E(V) = E_0 + \frac{9V_0B_0}{16}\left\{\left[\left(\frac{V_0}{V}\right)^{2/3} - 1\right]^3 B_0' + \left[\left(\frac{V_0}{V}\right)^{2/3} - 1\right]^2\left[6 - 4\left(\frac{V_0}{V}\right)^{2/3}\right]\right\} \quad (2)$$

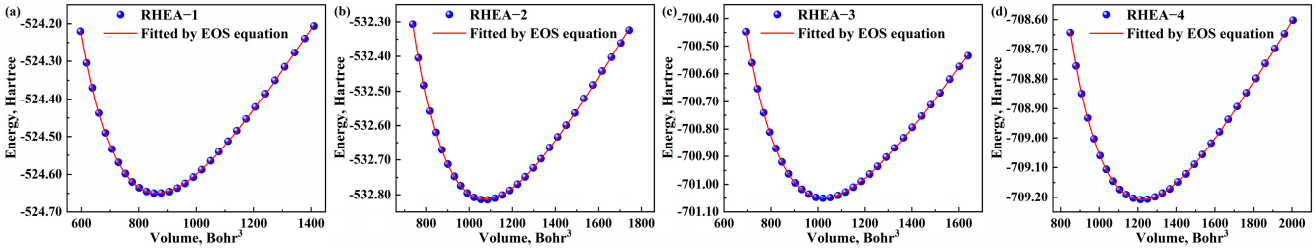

Figure 2. The relationship between energy and volume of RHEAs: (**a**) RHEA−1; (**b**) RHEA−2; (**c**) RHEA−3; (**d**) RHEA−4.

Among them, E_0 and V_0, respectively, represent the energy and volume of the equilibrium state (minimum system energy); B_0 is the bulk modulus at pressure $P = 0$; B_0' is the derivative of the bulk modulus relative to pressure; and V is the volume of change. The bulk modulus B_0 and its derivatives B_0' are usually obtained by fitting with experimental data, defined as Equation (3):

$$B_0 = -V\left(\frac{\partial P}{\partial V}\right)_{P=0},\ B_0' = -V\left(\frac{\partial B}{\partial P}\right)_{P=0} \quad (3)$$

Using OriginPro 2024b (Learning Edition) to analyze, fit, and plot these data points, obtain the energy volume fitting line shown by the red curve in Figure 2. The volume and energy of the equilibrium state SQS model obtained by EOS fitting are listed in Table 3.

Table 3. Volume and energy of equilibrium SQS model obtained by EOS fitting.

Parameter	RHEA−1	RHEA−2	RHEA−3	RHEA−4
E_0/Hartree	−524.64946	−532.813	−701.04846	−709.20839
V_0/Bohr^3	863.30459	1074.57045	1024.59003	1221.91889

Note: 1 Hartree ≈ 27.2114 eV; 1 Bohr ≈ 0.529177249 Å.

The CASTEP geometry optimization task allows for fine-tuning 3D periodic parameters to obtain stable structures. The exchange-correlation potential is described by using the generalized gradient approximation of Perdew–Burke–Ernzerhof (GGA-PBE), combined with the two point steepest descent (TPSD) algorithm and ultra soft pseudopotential (OTFG ultra soft) to perform geometric optimization on the structure [31,44]. The space group code for the SQS supercell model of the refractory high-entropy alloy shown in Figure 1 is P4MM (#99), which belongs to the tetragonal structure. After convergence testing and geometric optimization, the elastic constant C_{ij} of their equilibrium structures was calculated, and a strain pattern of 6 × 6 was set during the calculation. The elastic stability of the RHEA structural model is determined based on the necessary and sufficient conditions for the four elastic stability criteria of the square structure shown in Equation (4) using the calculated C_{ij} matrix data. The structure is elastic and stable when these conditions are met in the calculation results [45].

$$C_{11} > |C_{12}|,\ 2C_{13}^2 < C_{33}(C_{11} + C_{12}),\ C_{44} > 0,\ C_{66} > 0 \quad (4)$$

The single crystals C_{11}, C_{12}, and C_{44} with the cubic structure can be obtained using the averaging scheme proposed by Gao et al. [46], as listed in Equation (5).

$$\begin{cases} C_{11}(\text{bcc}) = \left.\frac{C_{11}+C_{22}+C_{33}}{3}\right|_{\text{SQS}} \\ C_{12}(\text{bcc}) = \left.\frac{C_{12}+C_{23}+C_{13}}{3}\right|_{\text{SQS}} \\ C_{44}(\text{bcc}) = \left.\frac{C_{44}+C_{55}+C_{66}}{3}\right|_{\text{SQS}} \end{cases} \quad (5)$$

According to the necessary and sufficient conditions of the Born Huang mechanical stability criterion [45], the average cubic single crystals C_{11}, C_{12}, and C_{44} must meet the requirements in Equation (6). (Note: C_{11}, C_{12}, and C_{44} listed in this paper are all corresponding values for the average cubic single crystals).

$$C_{11} - C_{12} > 0,\ C_{11} + 2C_{12} > 0,\ C_{44} > 0 \quad (6)$$

When the Cauchy pressure $C_p = C_{12}–C_{44}$ value is greater than 0, it indicates that the alloy structure is entirely metal-bonded [47]. The tetragonal shear modulus (C'), bulk modulus (B), shear modulus (S), Young's modulus (Y), and Poisson's ratio (v) of RHEAs all follow the Voigt Reuss Hill mean rule, and are defined as Equation (7) [45].

$$\begin{cases} C' = (C_{11} - C_{12})/2 \\ B = B_V = B_R = (C_{11} + 2C_{12})/3 \\ S_V = (C_{11} - C_{12} + 3C_{44})/5 \\ S_R = [5(C_{11} - C_{12})C_{44}]/[3(C_{11} - C_{12}) + 4C_{44}] \\ S = S_H = (S_V + S_R)/2 \\ Y = 9BS/(3B + S) \\ v = (3B - 2S)/(6B + 2S) \end{cases} \quad (7)$$

The shear anisotropy factor measures the degree of anisotropy in atomic bonding between planes [48]. The shear anisotropy coefficients of the (100) shear plane between <011> and <010> directions, the (010) shear plane between <101> and <001> directions, and the (001) shear plane between <110> and <010> directions are A_1, A_2, and A_3, respectively. For isotropic crystals, factors A_1, A_2, and A_3 must be 1, and any value less than or greater than 1 measures the degree of elastic anisotropy the crystal possesses. In a cubic structure $C_{11} = C_{22} = C_{33}$, $C_{44} = C_{55} = C_{66}$, $C_{12} = C_{23} = C_{13}$, then $A_1 = A_2 = A_3 = A_Z = 2C_{44}/(C_{11}–C_{12})$. Among them, A_Z is the Zener anisotropy index, which can quantify the anisotropy of cubic crystals [45]. G_V and G_R can also characterize polycrystalline solids formed by randomly oriented anisotropic single-crystal particles. In these quasi-isotropic materials, the measure of elastic anisotropy is defined as the A_{VR} Equation (S2); the universal anisotropy index A^U Equation (S3) [45], based on the extreme principle of elasticity and taking into account the elastic stiffness (or flexibility) tensor, applies to all types of elastic single crystals. For locally isotropic single crystals, the value of A^U is zero, and the magnitude of the deviation of A^U from zero defines the degree of anisotropy.

2.3. Thermodynamics Based on Quasi-Harmonic Approximation Model

The quasi-harmonic approximation (QHA) model proposed by A. Otero-de-la-Roza et al. [49] calculates the non-equilibrium Gibbs free energy by controlling the solid geometry at a given pressure and temperature:

$$G*(\boldsymbol{x}, V; p, T) = E_{static}(\boldsymbol{x}, V) + pV + F^*_{vib}(\boldsymbol{x}, V; T) + F^*_{el}(\boldsymbol{x}, V; T) + \cdots \quad (8)$$

Among them, E_{static} is the static energy of RHEAs (i.e., the equilibrium volume and energy of the structure calculated by CASTEP software); and F^*_{vib} is the non-equilibrium vibration Helmholtz free energy. The crystal structure is entirely determined by the volume V and several coordinates, including atomic positions and cell parameters, collectively

referred to as x here. More free energy terms represent additional degrees of freedom in solids, such as electrons (F_{el}^{*}), magnetism, configuration, defects, etc. The free energy $G(p, T)$, equilibrium entropy (S), Gibbs free energy (G), constant heat capacity (C_v), isothermal bulk modulus (B_T), Grüneisen parameter γ, thermal expansion coefficient α, constant heat capacity (C_p), and adiabatic bulk modulus (B_S) are calculated as Equations (S4)~(S7).

3. Results and Discussion

3.1. Structural Stability

3.1.1. Lattice Distortion

After first principles calculation and geometric optimization, the coordinate information of each atom in the SQS supercell structure models of the four RHEAs has undergone varying degrees of distortion, and the lattice vectors of all structures have changed, that is, the volume size of the structures has changed. There is only a slight (less than 0.51%) difference between the geometrically optimized structural volumes of the four RHEAs and the equilibrium volumes obtained from the EOS fitting curve, with differences of magnitude 0.29%, 0.51%, 0.37%, and 0.41%. Among them: $|\Delta V| = \left|\frac{V_{goe}-V_{EOS}}{V_{EOS}} \times 100\%\right|$. The equilibrium structure obtained after geometric optimization was calculated using the VESTA code [44] to obtain its powder diffraction data (i.e., XRD curve). The calculated XRD curve is shown in Figure 3. The XRD curve of the RHEA structure matches well with the NbV [50] in the PDF card library. The space group code of this card is Im-3m (229), a typical BCC structure space group code. These indicate that the four alloys have a BCC structure. The interplanar spacing and lattice constant of each phase in the RHEAs can be obtained from Bragg's law and its derived equations, such as Equation (S8).

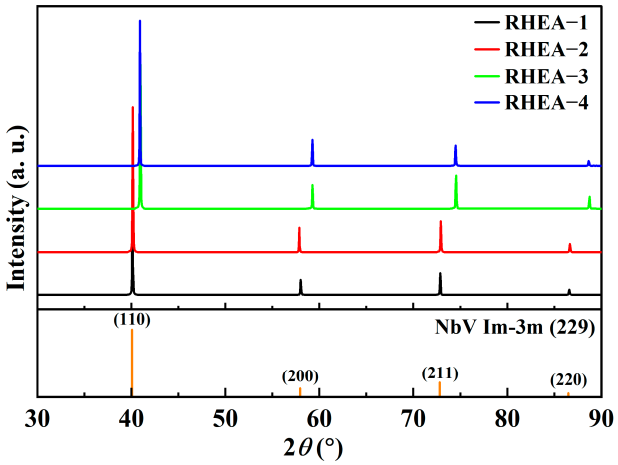

Figure 3. Comparison of XRD curves of RHEA structure after geometric optimization.

From the angle change of the theoretical XRD curve peak in Figure 3, it is found that the difference between RHEA-1, RHEA-2 alloys, and the NbV phase (PDF card data) [50] is relatively small. In contrast, the difference between RHEA-3 and RHEA-4 alloys is more significant. The diffraction peak 2θ angle difference corresponding to the crystal plane (220) in the RHEA-3 structure is the largest, reaching 2.258°, and the most negligible angle difference is the diffraction peak of the crystal plane (110) in the RHEA-1 structure, only 0.025°. The lattice constants and interplanar spacing of the four RHEAs are all smaller than the standard BCC NbV phase [50], and the order of magnitude of this change is RHEA-3 > RHEA-4 > RHEA-2 > RHEA-1. That is to say, the lattice constants of RHEA-2, RHEA-3, and RHEA-4 decrease relative to RHEA-1 while the interplanar spacing increases. The main reason for the difference in the calculated XRD data of the four RHEAs shown in Figure 3 is due to the distortion of the alloy structure caused by the addition of Al/Cr. The atomic radii of Al, Cr, and AlCr are $r_{\text{RHEA-2}}$ = 1.432 Å, $r_{\text{RHEA-3}}$ = 1.249 Å, and $r_{\text{RHEA-4}}$ = 1.341 Å, respectively (where $r_{\text{RHEA-4}} = (r_{\text{RHEA-2}} + r_{\text{RHEA-3}})/2$). Compared

with the theoretical atomic radius $r_{RHEA\text{-}1}$ of RHEA-1 ($r_{RHEA\text{-}1}$ = 1.393 Å), the $|\Delta r|$ value is 0.040 Å, 0.144 Å, and 0.052 Å, respectively. The degree of distortion relative to the RHEA-1 structure is RHEA-3 > RHEA-4 > RHEA-2.

3.1.2. Thermodynamic Stability

The enthalpy of formation and binding energy are commonly used to characterize the thermodynamic stability of alloy systems. The enthalpy of formation (or heat of formation) refers to the energy released by the system when atoms form compounds from a single substance (or substance) state, which can be used to characterize the difficulty of compound formation. When the value of heat formation is negative, and the absolute value of its value is more significant, it indicates that the substance is more likely to form [45]. The calculation formula for the enthalpy H_{form} (in eV/atom) of single-phase solid solution alloy formation is as Equation (S9) [45]. When calculating the energy of the elemental M structure, the same parameter settings as RHEA cell structure optimization are used. Figure 4a shows the enthalpy of formation H_{form} bar charts for four types of RHEA supercell structures with equal molar ratios. Figure 4a shows that the H_{form} of the four alloys are all negative, indicating that they are thermodynamically stable structures. However, with the addition of the Al element, the H_{form} of RHEA−2 (RHEA−4) is more negative than RHEA−1 (RHEA−3), indicating that they are more likely to form thermodynamically stable structures.

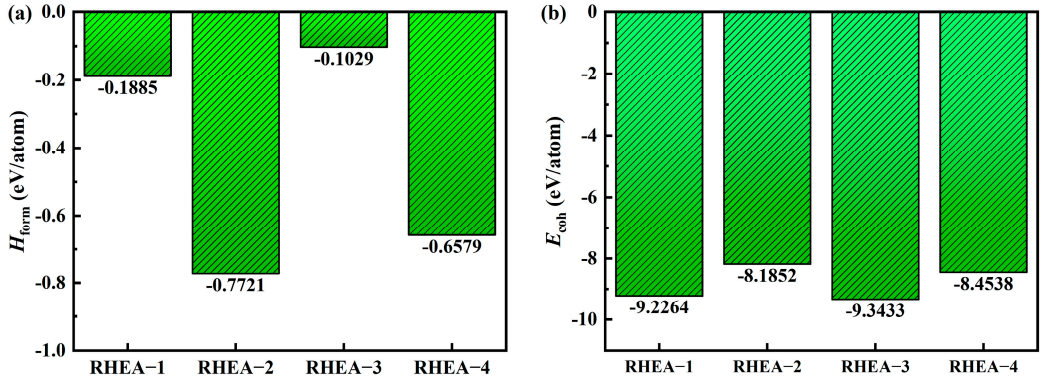

Figure 4. (**a**) The formation enthalpy H_{form}, and (**b**) the binding energy E_{coh} of the RHEAs.

Crystal binding energy is released by combining free atoms into a crystal, which is the minimum amount of external work required to decompose a crystal into individual atoms. When the binding energy is negative, the larger the absolute value, the more stable the crystal will be. The binding energy E_{coh} (in eV/atom) calculated by first principles is defined as Equation (S10) [45]. The E_{coh} bar chart of the four RHEA supercell structures is shown in Figure 4b. From Figure 4b, it can be seen that the E_{coh} values of the four alloy structures range from −8.1852 to −9.3433 eV/atom, while the E_{coh} value of the Ni_3Al alloy phase is only −4.3036 eV/atom [51]. Compared with the Ni_3Al alloy, more external work will be required to decompose the structures of the RHEA−1, RHEA−2, RHEA−3, and RHEA−4 alloys into individual atoms, indicating that these four alloy structures may have higher strength and more robust structural stability.

3.1.3. Elasticity Stability

The elastic constant matrices of four SQSs were calculated, and the lattice constants a, single crystal C_{11}, C_{12}, and C_{44} of the cubic structure were obtained by referring to the averaging scheme proposed by Gao et al. [46]. Based on this, the elastic stiffness, elastic constant C_{ij}, bulk modulus B, shear modulus S, Young's modulus Y, and Poisson's ratio v values were calculated, as shown in Table 4. The variation of C_{ij} values for the four RHEAs is shown in Figure 5. From Figure 5, it can be seen that their C_{ij} satisfies the Born Huang mechanical stability principle: $C_{11}, -C_{12} > 0$, $C_{11} + 2C_{12} > 0$, $C_{44} > 0$, indicating that the SQSs of these four al-

loys are mechanically stable. The order of the ability of the four RHEA structures to resist axial strain (C_{11}) is RHEA−3 > RHEA−2 > RHEA−1 > RHEA−4. The order of the ability to resist shear deformation (C_{44}) is RHEA−4 > RHEA−1 > RHEA−3 > RHEA−2. C_{12} represents the modulus that resists shear deformation along the [110] crystal direction on the (110) crystal plane, and their order of magnitude is RHEA−3 > RHEA−2 > RHEA−1 > RHEA−4.

Table 4. Lattice constant (a, Å) and elastic parameters of RHEAs (the units are GPa).

Parameter	RHEA−1	RHEA−2	RHEA−3	RHEA−4
a	3.177	3.175	3.116	3.117
C_{11}	243.914	256.536	273.205	238.983
C_{12}	127.084	128.388	132.683	120.564
C_{44}	39.823	27.338	32.676	50.257
C'	58.4152	64.074	70.261	59.209
C_p	87.262	101.050	100.007	70.307
B	166.027	171.104	179.524	160.037
S_V	47.260	42.032	47.710	53.838
S_R	45.632	35.473	41.571	53.492
S	46.446	38.756	44.641	53.6652
B/S	3.575	4.415	4.022	2.982
Y	127.453	108.097	123.672	144.809
v	0.372	0.395	0.385	0.349

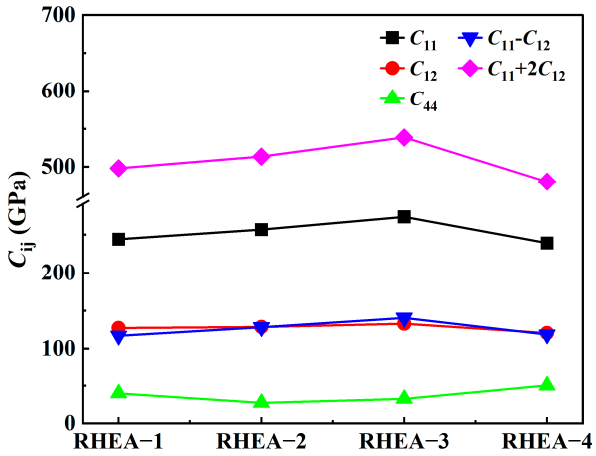

Figure 5. C_{ij} based on rheas supercell calculation.

3.2. Mechanical Property

3.2.1. Elastic Mechanical Properties

Copper (3.00), silver (3.44), palladium (4.27), and platinum (5.25) all have high *B/S* values, so they all have good ductility [45]. The *B/S* values of these four RHEAs are 3.575, 4.415, 4.022, and 2.982, respectively, indicating that they all have good ductility. As shown in Figure 6a, metals Al, Cr, Mo, Nb, Ti, V, and MoNbTaW-based refractory high-entropy alloys exhibit similar patterns.

In the BCC structure, C_{11} is the modulus parameter with the highest value among all independent elastic stiffness coefficients. When the Cauchy pressure C_p value is zero, that is, $C_{12} = C_{44}$, it indicates that atoms interact through the central force potential. Positive C_p indicates ductile metal bonding in the crystal, while negative values indicate covalent brittleness [45]. The C_p values of the four RHEA structures are positive, indicating that metal bonds bond the atoms in the structures and are ductile alloys. As shown in Figure 6b, the C_p values of Al, Cr, Mo, Nb, Ti, V, and MoNbTaW refractory high-entropy alloys are all located in the region of $C_{12} > C_{44}$, indicating that they are ductile materials bonded by metal bonds.

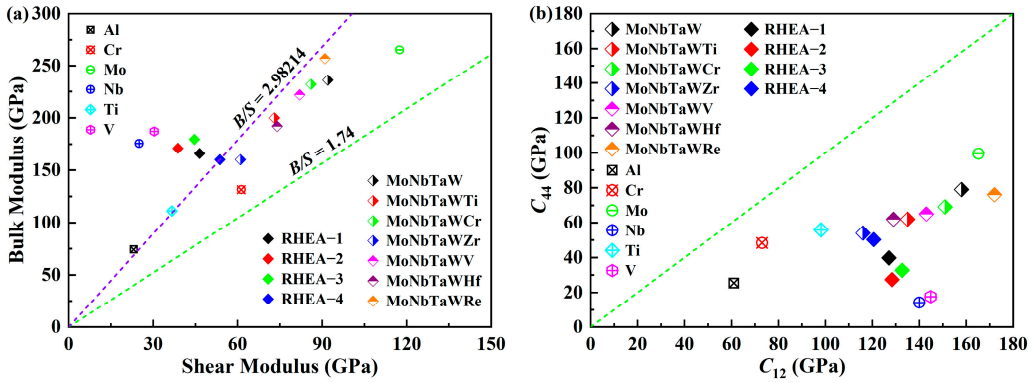

Figure 6. The distribution of *B*/*S* values of RHEAs. (**a**,**b**) The relative magnitudes of their elastic stiffness parameters C_{12} and C_{44}.

The Poisson's ratio v represents the relative values of solid compression (or tension) deformation and shear deformation. When the v of a material is more significant than 0.26, the material exhibits toughness, and the magnitude of toughness is positively correlated with the v [52]. The v of RHEAs in Table 4 are all greater than 0.26, indicating that their toughness is good. Figure 7 shows the *B*/*S* ratios of four RHEAs and their corresponding v. It can be found that there is a positive correlation between v and the *B*/*S* ratio. After simplifying the calculation equation describing the v in Equation (S1), the new Equation (9) can be obtained. From Equation (9), it can be seen that the v is positively correlated with the *B*/*S* ratio. These are consistent with the trend of change in Figure 7.

$$\begin{cases} v = (3B - 2S)/(6B + 2S) = (3B/S - 2)/(6B/S + 2) \\ v = \frac{1}{2} - \frac{3}{(6B/S+2)} \end{cases} \quad (9)$$

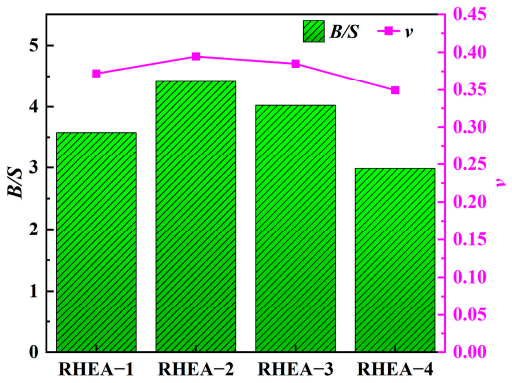

Figure 7. *B*/*S* ratio and its v of RHEAs.

The addition of alloying elements results in a change in the Y value. When Al or Cr is added individually, there is a decrease in the Y value. Conversely, the simultaneous addition of Al and Cr leads to an approximate increase of 13.62% in the Y value. This suggests that the process of alloying can significantly influence the material's stiffness to a certain degree. The ranking of the modulus Y values for the four alloys, from highest to lowest, is as follows: RHEA−4, RHEA−1, RHEA−3, and RHEA−2.

The elastic anisotropy of crystals is essential because it relates to the possibility of inducing microcracks in materials. The mechanical anisotropy of refractory high-entropy alloys is mainly represented by the Zener anisotropy factor A_Z (equivalent to shear anisotropy factors A_1, A_2, and A_3 in cubic crystals), elastic anisotropy factor A_{VR}, and universal anisotropy factor A^{U}. The calculated values of anisotropy factors for the four alloys are shown in Table 5. $A_Z \neq 1$ and $A_{VR} \neq 0$ indicate that they are all anisotropic materials. The A^{U} is a mechanical property anisotropy determination factor based on the extreme value principle of elastic mechanics, considering the elastic stiffness (or flexibility) tensor. The degree of

anisotropy of a material is consistent with its value trend. According to Table 5, the order of mechanical anisotropy for the four alloys is RHEA−2 > RHEA−3 > RHEA−1 > RHEA−4.

Table 5. Anisotropy index factor of the RHEAs.

Anisotropic Factor	RHEA−1	RHEA−2	RHEA−3	RHEA−4
A_Z	0.6817	0.4267	0.4651	0.8488
A_{VR}	0.0175	0.0846	0.0688	0.0032
A^U	0.1783	0.9245	0.7384	0.0323

Elastic anisotropy is related to the arrangement of atoms in different directions in a crystal structure so that a three-dimensional surface structure can directly characterize it. For cubic crystals, the anisotropy of bulk modulus B, shear modulus S, and Young's modulus Y can be calculated according to Equation (S11) [3]. In this representation, the isotropic system will appear spherical. Hence, the degree of deviation between the geometric body and the sphere represents the degree of anisotropy of specific properties of the system. The larger the deviation, the more pronounced the elastic anisotropy of the solid. Figure S1 shows that the modulus spheres of the four alloys are approximately completely spherical, indicating that their bulk modulus anisotropy is not significant and tends to be isotropic. Figure S2a–d shows that the shear modulus surfaces of the four alloys are irregular three-dimensional surfaces that deviate from the regular spherical shape, and the projection curves of the shear modulus 3D surfaces on three different low refractive index crystal planes (001), (110), and (111) have different deviations (in Figure S3). Based on these, it can be determined that the shear modulus anisotropy order of these four RHEAs alloys is RHEA-2 > RHEA-3 > RHEA-1 > RHEA-4. As shown in Figure S4a–d, the anisotropic 3D surfaces of Young's modulus (Y) of the four alloys are all irregular three-dimensional surfaces, indicating that their Y is significantly anisotropic. Based on the surface projection curve shown in Figure S5, the order of Y anisotropy for the four RHEA alloys can be determined as RHEA-2 > RHEA-3 > RHEA-1 > RHEA-4.

To better understand the mechanical anisotropy characteristics of RHEAs, Zhang et al. [53] proposed a universal formula Equation (S12) for calculating Young's modulus values of cubic crystals in different crystal orientations. The Young's modulus of RHEA single crystals in the standard directions of three low index crystal planes (001), (110), and (111) was calculated using Equation (S12). Their values are listed in Table 6. S_0 is also the flexibility anisotropy factor, and $S_0 = 0$ represents elastic isotropy. The S_0 of the four RHEAs and the calculated Y on [100], [010], and [001] are all listed in Table 6. The flexibility anisotropy factor $S_0 \neq 0$ for the four RHEAs indicates that they are all elastic anisotropic structures. The comparison between the calculated Y of RHEAs in different crystal orientations is listed in Table 6 and the intersection values of the modulus projection curve (Figure S5) shows that the values (or intersections) of the two methods tend to be consistent in the crystal orientations [100], [010], and [001].

Table 6. The S_0 and Young's modulus in different crystal directions of RHEAs (unit: GPa).

Alloys	S_0	[100]	[010]	[001]
RHEA−1	−0.0040	156.850	156.850	156.850
RHEA−2	−0.0105	170.891	170.891	170.891
RHEA−3	−0.0082	186.459	186.459	186.459
RHEA−4	−0.0015	158.128	158.128	158.128

According to the method proposed by Zhang et al. [53] for calculating the Poisson's ratio anisotropy of cubic crystals Equation (S13), 3D surface graphs of Poisson's ratio anisotropy for four RHEAs were plotted (Figure S6), as well as their Poisson's ratio distribution curves in the standard directions of the low index crystal planes (001), (110), and (111) (Figure S7), indicating that their v is anisotropic. The order of the difference between the

maximum and minimum values of the four RHEAs v in the standard directions of the low index crystal planes (001), (110), and (111) is RHEA−2 > RHEA−3 > RHEA−1 > RHEA−4. Figure S7 shows that the v shapes of four RHEAs are similar in the characteristic crystal direction (111), which is very similar to the anisotropy of Y. Both are represented by the combination Equation (S1) of B and S. The B of the four RHEAs in this article is isotropic; therefore, B in Equation (10) can be understood as a constant, indicating a specific linear correlation between Y and v. And the S has obvious anisotropy, there is a particular corresponding relationship between the S, Y, and v.

$$Y = 2S(1 + v) = 3B(1 + 2v) \quad (10)$$

3.2.2. Thermodynamic Performance

The static energy value curves of four RHEAs cubic structures obtained based on the QHA model [49] in the temperature range of 0–2000 K are shown in Figure 8. Figure 8a–d shows that the static energy values of the four RHEA cubic structures gradually increase with increasing temperature. These may be due to the increase in temperature, which increases the internal energy of atoms in the RHEA cubic structure (mainly the kinetic energy of atoms), thereby increasing the energy of the entire RHEA cubic structure system.

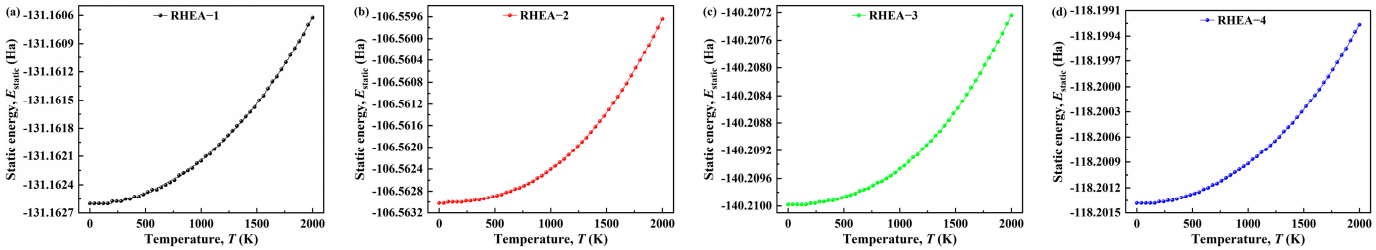

Figure 8. The static energy (E_{static}) of RHEAs in the temperature range of 0~2000 K: (**a**) RHEA−1; (**b**) RHEA−2; (**c**) RHEA−3; (**d**) RHEA−4.

Figure 9 shows the entropy curves of four RHEAs at different temperatures. The entropy values of these four RHEAs show a positive correlation trend with the increase in temperature; that is, as the system temperature increases, the degree of chaos gradually increases.

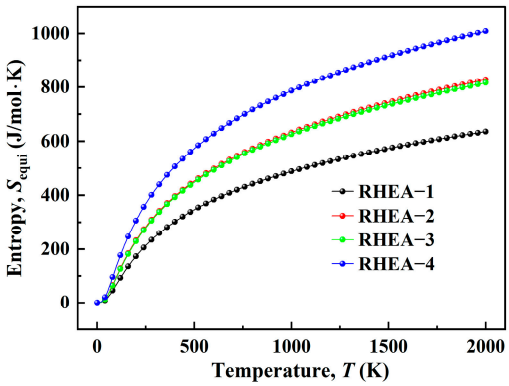

Figure 9. Entropy of RHEA cubic structure in the temperature range of 0~2000 K.

The trend of free energy changes for the four RHEA cubic structures in the temperature range of 0~2000 K is shown in Figure 10. From Figure 10a~d, it can be seen that there is no significant abrupt change in the slope of the temperature-dependent point lines for the free energy of the four alloys. From Figures 9 and 10, it can be seen that there is no significant change in the entropy and energy of RHEAs, indicating that the structures of the four RHEAs are stable and sound in the temperature range of 0–2000 K, without any phase transition.

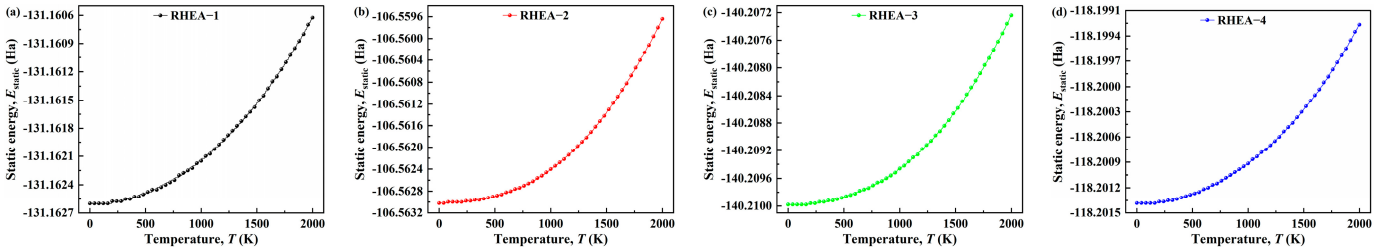

Figure 10. Gibbs free energy of RHEAs cubic structure in the temperature range of 0~2000 K: (**a**) RHEA−1; (**b**) RHEA−2; (**c**) RHEA−3; (**d**) RHEA−4.

Figure 11 shows the point and line plots of the constant heat capacity of the four RHEAs as a function of temperature. Figure 11a shows the temperature variation of C_v in the optimized SQS within the temperature range of 0–2000 K; Figure 11b shows the temperature variation of C_v in the cubic structure obtained by averaging the optimized SQS in the temperature range of 0–2000 K [46]. The C_v in Figure 11a,b both approach a specific limit infinitely with increasing temperature (as shown by the magenta dotted line in the figure), which is called the Dulong–Petit limit $C_v = 3\, n_{atoms} N_A k_B$ (n_{atoms} is the number of atoms contained in the structure; N_A is the Avogadro constant, with a value of 6.022×10^{23}; K_B is the Boltzmann constant, with a value of 1.380649×10^{-23} J/K) [54,55]. The SQSs of the four RHEAs mentioned in this article contain atomic numbers (i.e., n) of 8, 10, 10, and 12, respectively. Therefore, the Dulong–Petit limits C_v of the four alloys are 199.48 J·mol^{-1}·K^{-1}, 249.35 J·mol^{-1}·K^{-1}, 249.35 J·mol^{-1}·K^{-1}, and 299.21 J·mol^{-1}·K^{-1}, respectively, as shown by the magenta dotted line in Figure 11a. The equivalent cubic structures of the four RHEAs contain only two atoms, i.e., $n_{atoms} = 2$, resulting in an equivalent Dulong–Petit limit C_v of 49.89 J·mol^{-1}·K^{-1}, as shown by the magenta dashed line in Figure 11b.

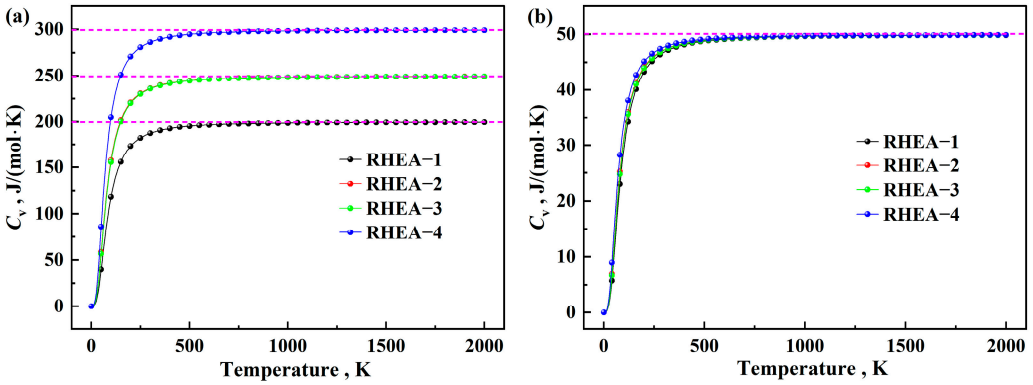

Figure 11. The dot-line diagram of the C_v of RHEAs as a function of temperature: (**a**) SQS model; (**b**) equivalent cubic structure.(Pink line: It represents the Dulong–Petit limits C_v).

Figure 12 shows the point line graph of the constant pressure heat capacity of four RHEAs as a function of temperature. Figure 12a shows the variation of C_p with temperature in the temperature range of 0–2000 K for the SQSs of the four RHEAs; Figure 12b shows the temperature variation of C_p in the cubic structure obtained by averaging the optimized SQS [47] in the temperature range of 0–2000 K. The difference in heat capacity values among these four RHEAs is significant (as shown in Figures 11 and 12), and the underlying reason is mainly attributed to their structural differences. According to the equipartition of energy theorem [56], diatomic molecules can have twice the kinetic energy of monatomic matter at the same temperature. In other words, the specific heat per mole of diatomic molecular matter is twice that of monatomic matter. Therefore, more complex molecules have higher molar specific heat. Due to the atomic ratio of the SQSs of the four RHEAs being 8:10:10:12, there is an approximate ratio difference in their C_v and C_p specific heats, as shown in Figures 11a and 12a. The number of atoms in the equivalent cubic structure is

2, so the particular C_v and C_p heat values tend to be consistent (or have minor differences), as shown in Figures 11b and 12b.

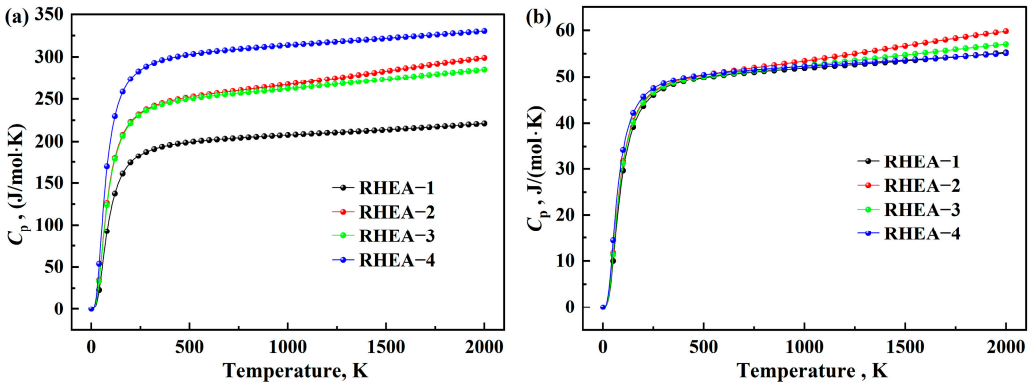

Figure 12. The dot-line diagram of the C_p of RHEAs as a function of temperature: (**a**) SQS model; (**b**) equivalent cubic structure.

The higher the coefficient of thermal expansion (CTE) of a material, the more it will expand during heating reactions. CTE usually has two types: linear expansion coefficient (α_l) and volume expansion coefficient (α_v). Moreover, there is an approximate proportional relationship of $\alpha_v \approx 3\alpha_l$. Figure 13 shows the temperature-dependent plot of the volumetric thermal expansion coefficients of the four RHEAs and two titanium alloys α-Ti and β-Ti. The growth rate of the α_v of all alloys in the figure is significantly higher than that above room temperature before the temperature drops below 298 K, and they are all within the same order of magnitude range. Among them, the MoNbTiV alloy gradually increases in a flat trend above 298 K, while the growth trend of the RHEA-3 alloy is slightly higher than that of MoNbTiV. The RHEA-4 alloy gradually increases to its maximum value (3.1744×10^{-5}/K) and then has a slightly decreasing range (520–835 K) before gradually increasing again. The trend of α_v variation with temperature is very similar for RHEA-2 and the two titanium alloys, α-Ti and β-Ti. The difference is that the α_v of RHEA-2 shows a decreasing trend after reaching its maximum value (4.5985×10^{-5}/K).

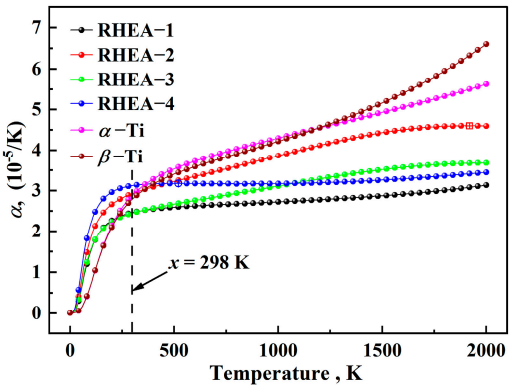

Figure 13. Point line diagram of the α_v for RHEAs and α-Ti, β-Ti in the temperature range of 0~2000 K.

To provide support for the subsequent laser cladding preparation of RHEA coatings (RHEACs), the difference between the α_v of these four RHEAs and α-Ti, or β-Ti, was calculated with temperature and plotted as shown in Figure 14. Figure 14a shows the difference curve between the α_v of RHEAs and α-Ti with temperature, and the range of the $\Delta\alpha_v$ is -2.4896~1.4993×10^{-5}/K. As shown in Figure 14b, the $\Delta\alpha_v$ between RHEAs and β-Ti ranges from -3.4693~1.4922×10^{-5}/K, then $|\Delta\alpha_v| < 3.47 \times 10^{-5}$/K. By combining $\alpha_v \approx 3\alpha_l$, the difference in α_l between RHEAs and the two titanium alloys can be obtained

$\Delta\alpha_1 < 1.16 \times 10^{-5}$/K. In summary, it indicates that the CTE of these RHEAs is relatively close to that of both α-Ti and β-Ti.

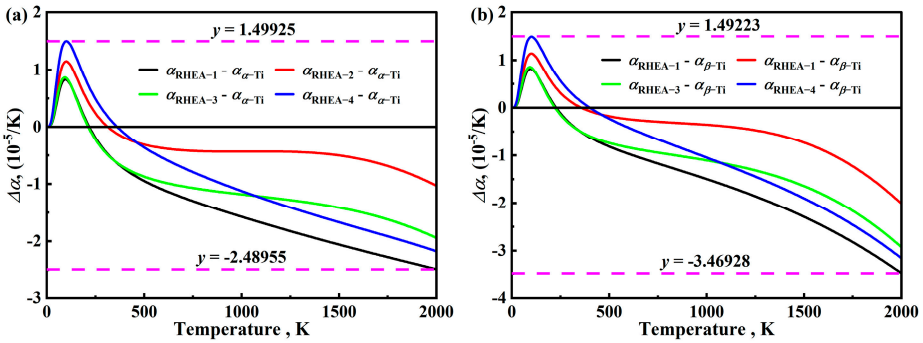

Figure 14. The curves of the α_V of the four RHEAs and the difference between α-Ti and β-Ti in the temperature range of 0~2000 K: (**a**) $\alpha_{V(RHEAs)} - \alpha_{V(\alpha\text{-Ti})}$; (**b**) $\alpha_{V(RHEAs)} - \alpha_{V(\beta\text{-Ti})}$.

4. Laser Cladding of Coatings

Based on the results of first principles calculations, pure metal elemental powders of Al, Cr, Mo, Nb, Ti, and V were used as raw materials. The purity of the metal powders was greater than 99.5% (wt.%), and the particle size of the powders was in the range of 30–60 μm. The metal powders were provided by Beijing Yanbang New Materials Technology Co., Ltd. (Beijing, China). The mixed metal powders of MoNbTiV, AlMoNbTiV, CrMoNbTiV, and AlCrMoNbTiV were weighed and prepared with near equimolar atomic ratios, and ball milled to mix the powders evenly. The mixed alloy powders were prefabricated into long strips measuring 90 mm × 4 mm × 1.5 mm, which were placed in the center of the surface of a clean-surface Ti-6Al-4V (TC4) alloy substrate measuring 90 mm × 10 mm × 4 mm (Baoji Titanium Co., Ltd., Baoji, China), as shown in Figure S8. The prefabricated specimens were placed in a drying oven at a temperature of 60 °C for 8 h to remove the residual moisture in the mixed metal powders and were kept in reserve.

The light source for the laser cladding was a GS-TEL-6000A 6 kW multimode constant current CO_2 laser, with the laser power set to 3.7 kW and the laser scanning speed set to 600 mm/min. To prevent oxidation during the deposition process, an argon atmosphere with an oxygen and moisture content of less than 10 ppm was required to protect the entire laser cladding process. A continuous flow of pure argon gas (argon purity of 99.99%, flow rate of 0.417 L/s) injected through a coaxial nozzle was used as the shielding gas. The parameters of the laser cladding process are in line with the previous work of the researcher [57].

The phase composition of the laser-fused RHEA coatings was characterized using an Empyrean Cu target (λ = 1.5406 Å) X-ray diffraction (XRD) instrument (PANalytical, Almelo, The Netherlands). The XRD tests were carried out at room temperature by scanning the test surface of the samples at a speed of 5°/min in the range of 30°~90°. A ZEISS EVO tungsten filament scanning electron microscope (SEM) was used to observe the morphology of the physical phase organization of the coatings. At the same time, an energy dispersive spectrometer (EDS) in SEM configuration was also used to perform line and surface sweeps to determine the distribution of Al, Cr, Mo, Nb, Ti, and V elements in the coating organization.

The XRD curves of the four RHEA coatings are shown in Figure 15. Figure 15a shows the XRD curves of the RHEA-1 coating, which corresponds well with the standard PDF card of the body-centered cubic structure $Nb_{0.5}Mo_{0.5}$ (Cubic $Im\bar{3}m$-229) [58]. It can be inferred that this phase is a typical BCC structure, indicating that the RHEA-1 coating is a single BCC-disordered solid solution structure. Figure 15b shows the XRD curves of the RHEA-2 coating, and it corresponds to the standard PDF card for $Ti_{0.5}V_{0.5}$ (Cubic $Im\bar{3}m$-229) [59]. Similarly, it indicates that the RHEA-2 coating also has a single BCC-disordered solid solution structure; Figure 15c shows the XRD curves of the RHEA-3 coating, and it

corresponds to the standard PDF card for NbV (Cubic Im$\bar{3}$m-229) [50] and Cr_2Nb (Cubic Fd-3m-227) [60], which correspond to the BCC phase and C15 Laves phase (Cr_2Nb type), respectively. This indicates that the RHEA-3 coating is composed of the main phase of BCC structural solid solution and a small amount of C15 Laves phase; Figure 15d shows the XRD curve of the RHEA-4 coating, corresponding to the standard PDF card for $Ti_{0.5}V_{0.5}$ (Cubic Im$\bar{3}$m-229) [61] and Cr_2Nb (Cubic Fd-3m-227) [60]. Similarly, it indicates that the RHEA-4 coating is composed of the main phase of BCC and a small amount of the C15 Laves phase.

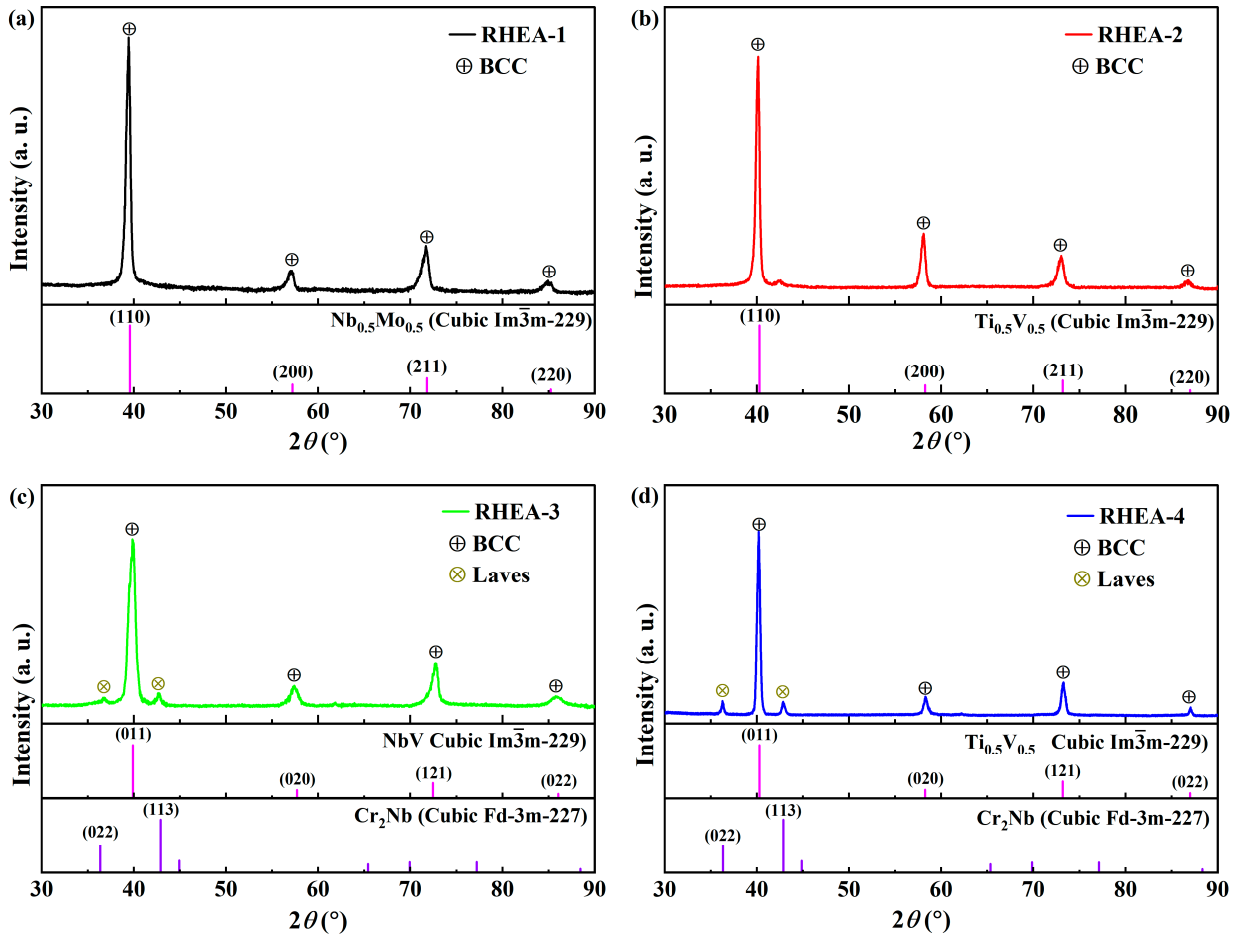

Figure 15. XRD curves of the four RHEA coatings: (**a**) RHEA−1, (**b**) RHEA−2, (**c**) RHEA−3, and (**d**) RHEA−4.

Figure 16 illustrates the scanning electron microscope (SEM) images of the bonding regions between the four types of RHEA coatings and the Ti-6Al-4V substrate. The images demonstrate that the bonding regions of the coatings with the titanium alloy substrate are metallurgically bonded, indicating that the four types of RHEAs have been successfully deposited on the Ti-6Al-4V substrate through laser cladding. This confirms that the expected RHEA coatings were obtained. The width (W, μm), height (H, μm), and substrate depth (h, μm) dimensions of the RHEA coatings can be obtained by adding auxiliary lines to the cross-sectional images of the RHEA coatings and substrate using Microsoft PowerPoint software, in combination with the SEM image scale. Subsequently, the geometric dilution of the coating's macroscopic morphology can be calculated. The corresponding geometrical dilutions of the coatings are 40.06%, 43.48%, 53.61%, and 35.05%, respectively. These high geometrical dilutions are primarily attributable to the significant concentration differential between Ti in the TC4 substrate and Ti in the RHEAs coatings, as well as the high solubility of Ti in refractory metals.

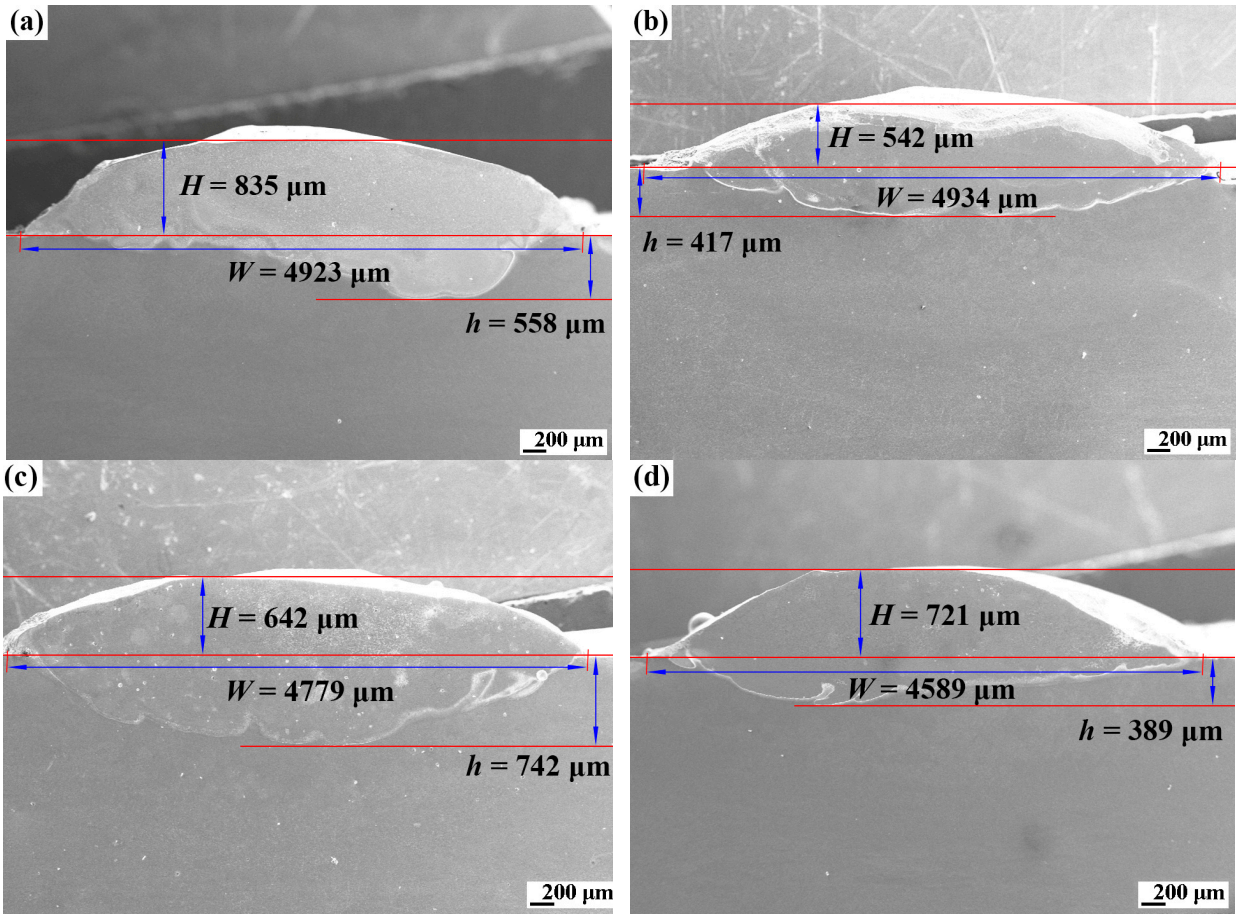

Figure 16. SEM image of the bonding zone between RHEA coatings and TC4 alloy substrate: (**a**) RHEA−1, (**b**) RHEA−2, (**c**) RHEA−3, and (**d**) RHEA−4.

5. Conclusions

Four equiatomic ratios of MoNbTiV, AlMoNbTiV, CrMoNbTiV, and AlCrMoNbTiV lightweight RHEAs were designed, and the effects of the Al/Cr alloying elements on the crystal structure, elastomechanical, and thermomechanical properties of the lightweight RHEAs were calculated using first principles. In addition, metallurgically bonded RHEA coatings were successfully obtained on Ti-6Al-4V substrates using laser cladding technology, and the following conclusions were drawn:

(1) First principles calculations show that the four RHEA alloys have stable equilibrium BCC structures, with theoretical densities of 7.358 g/cm^3, 6.409 g/cm^3, 7.331 g/cm^3, and 6.510 g/cm^3, respectively.

(2) The calculation of XRD data shows that the addition of Al/Cr alloy elements can cause distortion in the structure of the MoNbTiV alloy, and the lattice distortion is most apparent when the Cr element is added alone; the lattice constants of the four RHEAs are 3.177 Å, 3.175 Å, 3.116 Å, and 3.118 Å, respectively.

(3) The results of the elastic mechanics calculations show that the four RHEAs exhibit elastic anisotropy and their ductile structures. The order of magnitude for calculating Young's modulus and hardness values is AlCrMoNbTiV > MoNbTiV > CrMoNbTiV > AlMoNbTiV.

(4) Using the QHA model to calculate the thermal expansion coefficients of the four RHEAs, α-Ti and β-Ti are relatively close, with a difference in linear expansion coefficients less than 1.16×10^{-5}/K, indicating their potential as surface coating materials for titanium alloys.

(5) Metallurgically bonded RHEA coatings have been successfully obtained on Ti-6Al-4V substrates using laser cladding technology, and all four coatings have typical BCC solid solution phases (the CrMoNbTiV and AlCrMoNbTiV coatings contain a small amount of the second phase of C15 Laves), demonstrating that the methodology of designing laser cladding coatings using first principles calculations is scientifically feasible.

Supplementary Materials: The following supporting information can be downloaded at: https://www.mdpi.com/article/10.3390/coatings14111399/s1, Figure S1: 3D spherical graph of bulk modulus (B) for RHEAs: (a) RHEA−1; (b) RHEA−2; (c) RHEA−3; (d) RHEA−4; Figure S2: 3D spherical graph of shear modulus (S) for RHEAs: (a) RHEA−1; (b) RHEA−2; (c) RHEA−3; (d) RHEA−4; Figure S3: Projection curves of the 3D shear modulus anisotropic surfaces for four RHEAs on different crystal planes: (a) (001), (b) (110), and (c) (111).; Figure S4: Anisotropic 3D surface of Young's modulus (Y) for RHEAs: (a) RHEA−1; (b) RHEA−2; (c) RHEA−3; (d) RHEA−4; Figure S5: Projection curves of the 3D Young's modulus anisotropic surfaces for four RHEAs on different crystal planes: (a) (001), (b) (110), and (c) (111); Figure S6: Anisotropic 3D surface of Poisson's ratio for RHEAs: (a) RHEA−1; (b) RHEA−2; (c) RHEA−3; (d) RHEA−4; Figure S7: Projection curves of the 3D Poisson's ratio anisotropic surfaces for four RHEAs on different crystal planes: (a) (001), (b) (110), and (c) (111); Figure S8: TC4 alloy substrate and preset powder.; Table S1. The physical meanings of each symbol are in Table 1.

Author Contributions: L.C. and W.L.: writing—original draft; formal analysis. W.S.: execution of calculations. L.L.: algorithm design and model construction. J.S.: formal analysis. C.Y.: execution of calculations. J.Y.: visualization. X.Z. (Xuming Zhang) and P.Q.: formal analysis. A.C.: writing—review and editing. X.Z. (Xiaowei Zhang) and H.L.: writing—review and editing; funding acquisition. All authors have read and agreed to the published version of the manuscript.

Funding: This work was supported by the National Natural Science Foundation of China (grant number 61963021), Baise Municipal Science and Technology Research Program (grant number 20222007, 20230557), Guangxi Key Technologies R&D Program (grant number: AB23075104) and Baise Municipal Central Government Leading Local Science and Technology Development Fund Project (grant number 20224504).

Institutional Review Board Statement: Not applicable.

Informed Consent Statement: Not applicable.

Data Availability Statement: The raw data supporting the conclusions of this article will be made available by the authors on request.

Conflicts of Interest: Author Chengchu Yin was employed by the company Guangxi Zhongke Petrochemical Research Institute Testing Co., Ltd. The remaining authors declare that the research was conducted in the absence of any commercial or financial relationships that could be construed as a potential conflict of interest.

References

1. Philip, J.T.; Mathew, J.; Kuriachen, B. Tribology of Ti6Al4V: A review. *Friction* **2019**, *7*, 497–536. [CrossRef]
2. Dai, J.; Zhu, J.; Chen, C.; Weng, F. High temperature oxidation behavior and research status of modifications on improving high temperature oxidation resistance of titanium alloys and titanium aluminides: A review. *J. Alloys Compd.* **2016**, *685*, 784–798. [CrossRef]
3. Sienkiewicz, J.; Kuroda, S.; Murakami, H.; Araki, H.; Giżyński, M.; Kurzydłowski, K.J. Fabrication and Oxidation Resistance of TiAl Matrix Coatings Reinforced with Silicide Precipitates Produced by Heat Treatment of Warm Sprayed Coatings. *J. Therm. Spray Technol.* **2018**, *27*, 1165–1176. [CrossRef]
4. Zhang, L.-C.; Chen, L.-Y.; Wang, L. Surface Modification of Titanium and Titanium Alloys: Technologies, Developments, and Future Interests. *Adv. Eng. Mater.* **2020**, *22*, 1901258. [CrossRef]
5. Chen, K.; Liu, X.; Liu, X.; Meng, T.; Guo, Q.; Wang, Z.; Lin, N. Microstructure and wear behavior of Ti-6Al-4V treated by plasma Zr-alloying and plasma nitriding. *J. Wuhan Univ. Technol. Mater. Sci. Ed.* **2016**, *31*, 1086–1092. [CrossRef]
6. Zubkins, M.; Arslan, H.; Bikse, L.; Purans, J. High power impulse magnetron sputtering of Zn/Al target in an Ar and Ar/O_2 atmosphere: The study of sputtering process and AZO films. *Surf. Coat. Technol.* **2019**, *369*, 156–164. [CrossRef]
7. Wang, Y.; Yu, H.; Chen, C.; Zhao, Z. Review of the biocompatibility of micro-arc oxidation coated titanium alloys. *Mater. Des.* **2015**, *85*, 640–652. [CrossRef]

8. Movassagh-Alanagh, F.; Abdollah-zadeh, A.; Aliofkhazraei, M.; Abedi, M. Improving the wear and corrosion resistance of Ti–6Al–4V alloy by deposition of TiSiN nanocomposite coating with pulsed-DC PACVD. *Wear* **2017**, *390*, 93–103. [CrossRef]
9. Jie, J.; Zhou, S.; Zheng, D. The Corrosion Behavior and Mechanical Properties of fluorine doped hydroxyapatite/Micro-arc oxidation (MAO) composite coating on the pure titanium substrate using a combination of micro-arc oxidation and electrochemical deposition method. *Rare Met. Mater. Eng.* **2019**, *48*, 1725–1733.
10. Zhao, P.; Li, J.; Zhang, Y.; Li, X.; Xia, M.M.; Yuan, B.G. Wear and high-temperature oxidation resistances of AlNbTaZrx high-entropy alloys coatings fabricated on Ti6Al4V by laser cladding. *J. Alloys Compd.* **2021**, *862*, 158405. [CrossRef]
11. Kusinski, J.; Kac, S.; Kopia, A.; Radziszewska, A.; Rozmus-Górnikowska, M.; Major, B.; Major, L.; Marczak, J.; Lisiecki, A. Laser modification of the materials surface layer—A review paper. *Bull. Pol. Acad. Sci. Tech. Sci.* **2012**, *60*, 711–728. [CrossRef]
12. Huang, C.; Zhang, Y.; Vilar, R.; Shen, J. Dry sliding wear behavior of laser clad TiVCrAlSi high entropy alloy coatings on Ti–6Al–4V substrate. *Mater. Eng.* **2012**, *41*, 338–343. [CrossRef]
13. Xia, M.; Liu, A.; Hou, Z.; Li, N.; Chen, Z.; Ding, H. Microstructure growth behavior and its evolution mechanism during laser additive manufacture of in-situ reinforced (TiB+TiC)/Ti composite. *J. Alloys Compd.* **2017**, *728*, 436–444. [CrossRef]
14. Weng, F.; Yu, H.; Liu, J.; Chen, C.; Dai, J.; Zhao, Z. Microstructure and wear property of the Ti_5Si_3/TiC reinforced Co-based coatings fabricated by laser cladding on Ti-6Al-4V. *Opt. Laser Technol.* **2017**, *92*, 156–162. [CrossRef]
15. Yan, H.; Liu, K.; Zhang, P.; Zhao, J.; Qin, Y.; Lu, Q.; Yu, Z. Fabrication and tribological behaviors of Ti_3SiC_2/Ti_5Si_3/TiC/Ni-based composite coatings by laser cladding for self-lubricating applications. *Opt. Laser Technol.* **2020**, *126*, 106077. [CrossRef]
16. Zhou, Z.; Liu, X.-B.; Zhuang, S.-G.; Wang, M.; Luo, Y.-S.; Tu, R.; Zhou, S.-F. Laser in-situ synthesizing Ti_5Si_3/Al_3Ni_2 reinforced Al_3Ti/NiTi composite coatings: Microstructure, mechanical characteristics and oxidation behavior. *Opt. Laser Technol.* **2019**, *109*, 99–109. [CrossRef]
17. Yeh, J.W.; Chen, S.K.; Lin, S.J.; Gan, J.Y.; Chin, T.S.; Shun, T.T.; Tsau, C.H.; Chang, S.Y. Nanostructured High-Entropy Alloys with Multiple Principal Elements: Novel Alloy Design Concepts and Outcomes. *Adv. Eng. Mater.* **2004**, *6*, 299–303. [CrossRef]
18. Yao, H.; Qiao, J.; Gao, M.; Hawk, J.; Ma, S.; Zhou, H. MoNbTaV Medium-Entropy Alloy. *Entropy* **2016**, *18*, 189. [CrossRef]
19. Senkov, O.N.; Wilks, G.B.; Miracle, D.B.; Chuang, C.P.; Liaw, P.K. Refractory high-entropy alloys. *Intermetallics* **2010**, *18*, 1758–1765. [CrossRef]
20. Senkov, O.N.; Miracle, D.B.; Chaput, K.J.; Couzinie, J.-P. Development and exploration of refractory high entropy alloys—A review. *J. Mater. Res.* **2018**, *33*, 3092–3128. [CrossRef]
21. Han, L.; Ling-ling, M.; Chao-qun, W.; Lin, S.; Wei-ping, Z. Microstructure and Properties of Laser Cladding AlBxCoCrNiTi High-entropy Alloy Coating on Titanium Alloys. *Surf. Technol.* **2017**, *46*, 226–231.
22. Wu, G.; Wang, X.; Zeng, X.; Wang, A.; Xiong, D. Microstructure and properties of laser clad $AlCoCrFeNiTi_{0.5}$ high-entropy alloy coating on TC4 surface. *Heat Treat. Met.* **2019**, *44*, 1–5.
23. Cai, Z.B.; Pang, X.J.; Cui, X.F.; Wen, X.; Liu, Z.; Dong, M.L.; Li, Y.; Jin, G. In Situ Laser Synthesis of High Entropy Alloy Coating on Ti-6Al-4V Alloy: Characterization of Microstructure and Properties. *Mater. Sci. Forum* **2017**, *898*, 643–650. [CrossRef]
24. Cai, Z.; Jin, G.; Cui, X.; Liu, Z.; Zheng, W.; Li, Y.; Wang, L. Synthesis and microstructure characterization of Ni-Cr-Co-Ti-V-Al high entropy alloy coating on Ti-6Al-4V substrate by laser surface alloying. *Mater. Charact.* **2016**, *120*, 229–233. [CrossRef]
25. Cai, Z.; Cui, X.; Jin, G.; Lu, B.; Zhang, D.; Zhang, Z. In situ TEM tensile testing on high-entropy alloy coating by laser surface alloying. *J. Alloys Compd.* **2017**, *708*, 380–384. [CrossRef]
26. Xiang, K.; Chen, L.-Y.; Chai, L.; Guo, N.; Wang, H. Microstructural characteristics and properties of CoCrFeNiNbx high-entropy alloy coatings on pure titanium substrate by pulsed laser cladding. *Appl. Surf. Sci.* **2020**, *517*, 146214. [CrossRef]
27. Senkov, O.N.; Wilks, G.B.; Scott, J.M.; Miracle, D.B. Mechanical properties of Nb25Mo25Ta25W25 and V20Nb20Mo20Ta20W20 refractory high entropy alloys. *Intermetallics* **2011**, *19*, 698–706. [CrossRef]
28. Lo, K.-C.; Murakami, H.; Yeh, J.-W.; Yeh, A.-C. Oxidation behaviour of a novel refractory high entropy alloy at elevated temperatures. *Intermetallics* **2020**, *119*, 106711. [CrossRef]
29. Xiao, F.; Ruan, Z.; Chen, R.; Yin, W.; Fan, T. First-Principles Calculations on Relative Energetic Stability, Mechanical, and Thermal Properties of B2-AlRE (RE = Sc, Y, La-Lu) Phases. *Coatings* **2024**, *14*, 1346. [CrossRef]
30. Wang, Y.; Liu, H.; Hao, X.; Yang, C.; Liu, Y.; Chen, L.; Zhang, X. First-principles calculations to investigate phase stability, elastic and thermodynamic properties of TiMoNbX (X = Cr, Ta, Cr and Ta) refractory high entropy alloys. *J. Phys. Condens. Matter* **2024**, *36*, 485902. [CrossRef]
31. Wang, M.; Zhou, Y.; Tian, W.; Li, J.; Chen, H.; Tan, J.; Chen, X. First-principles study the mechanical, electronic, and thermodynamic properties of Mg-Al-Mn ternary compounds. *Vacuum* **2023**, *213*, 112140. [CrossRef]
32. Huang, C.; Zhang, Y.; Shen, J.; Vilar, R. Thermal stability and oxidation resistance of laser clad TiVCrAlSi high entropy alloy coatings on Ti–6Al–4V alloy. *Surf. Coat. Technol.* **2011**, *206*, 1389–1395. [CrossRef]
33. Murty, B.S.; Yeh, J.W.; Ranganathan, S. *High-Entropy Alloys*; Elsevier Inc.: Amsterdam, The Netherlands, 2014.
34. GUO, S.; LIU, C.T. Phase stability in high entropy alloys: Formation of solid-solution phase or amorphous phase. *Prog. Nat. Sci. Mater. Int.* **2011**, *21*, 433–446. [CrossRef]
35. Yang, X.; Zhang, Y. Prediction of high-entropy stabilized solid-solution in multi-component alloys. *Mater. Chem. Phys.* **2012**, *132*, 233–238. [CrossRef]
36. Guo, S.; Ng, C.; Lu, J.; Liu, C.T. Effect of valence electron concentration on stability of fcc or bcc phase in high entropy alloys. *J. Appl. Phys.* **2011**, *109*, 103505. [CrossRef]

37. Dong, Y.; Lu, Y.; Jiang, L.; Wang, T.; Li, T. Effects of electro-negativity on the stability of topologically close-packed phase in high entropy alloys. *Intermetallics* **2014**, *52*, 105–109. [CrossRef]
38. Clark, S.J.; Segall, M.D.; Pickard, C.J.; Hasnip, P.J.; Probert, M.I.J.; Refson, K.; Payne, M.C. First principles methods using CASTEP. *Z. Für Krist.-Cryst. Mater.* **2005**, *220*, 567–570. [CrossRef]
39. Zunger, A.; Wei, S.; Ferreira, L.G.; Bernard, J.E. Special quasirandom structures. *Phys. Rev. Lett.* **1990**, *65*, 353–356. [CrossRef]
40. Gao, M.C.; Yeh, J.-W.; Liaw, P.K.; Zhang, Y. *High-Entropy Alloys: Fundamentals and Applications*; Springer: Cham, Switzerland, 2016.
41. van de Walle, A.; Tiwary, P.; de Jong, M.; Olmsted, D.L.; Asta, M.; Dick, A.; Shin, D.; Wang, Y.; Chen, L.Q.; Liu, Z.K.; et al. Efficient stochastic generation of special quasirandom structures. *Calphad* **2013**, *42*, 13–18. [CrossRef]
42. Hu, Y.L.; Bai, L.H.; Tong, Y.G.; Deng, D.Y.; Liang, X.B.; Zhang, J.; Li, Y.J.; Chen, Y.X. First-principle calculation investigation of NbMoTaW based refractory high entropy alloys. *J. Alloys Compd.* **2020**, *827*, 153963. [CrossRef]
43. Momma, K.; Izumi, F. VESTA 3for three-dimensional visualization of crystal, volumetric and morphology data. *J. Appl. Crystallogr.* **2011**, *44*, 1272–1276. [CrossRef]
44. Chen, L.; Hao, X.; Wang, Y.; Zhang, X.; Liu, H. First-principles calculation of the effect of Ti content on the structure and properties of TiVNbMo refractory high-entropy alloy. *Mater. Res. Express* **2020**, *7*, 106516. [CrossRef]
45. Chong, X. Design of Microstructure and Investigation of Properties of the Reinforced Phases in Wear-Resistant Steel. Ph.D. Thesis, Faculty of Materials Science and Engineering, Kunming University of Science and Technology, Kunming, China, 2017.
46. Gao, M.C.; Suzuki, Y.; Schweiger, H.; Dogan, O.N.; Hawk, J.; Widom, M. Phase stability and elastic properties of Cr-V alloys. *J. Phys. Condens. Matter* **2013**, *25*, 075402. [CrossRef] [PubMed]
47. Mouhat, F.; Coudert, F.-X. Necessary and sufficient elastic stability conditions in various crystal systems. *Phys. Rev. B* **2014**, *90*, 224104. [CrossRef]
48. Ravindran, P.; Fast, L.; Korzhavyi, P.A.; Johansson, B.; Wills, J.; Eriksson, O. Density functional theory for calculation of elastic properties of orthorhombic crystals: Application to $TiSi_2$. *J. Appl. Phys.* **1998**, *84*, 4891–4904. [CrossRef]
49. Otero-de-la-Roza, A.; Abbasi-Pérez, D.; Luaña, V. Gibbs2: A new version of the quasiharmonic model code. II. Models for solid-state thermodynamics, features and implementation. *Comput. Phys. Commun.* **2011**, *182*, 2232–2248. [CrossRef]
50. Richter, K.-H.; Weiss, A. 1H-NMR Studies of the Systems Ta1−VH ($0.0 \leq x$ 2264 1.0; $0 < y \leq 0.9$), and Nb1−VH ($0.0 \leq x \leq 0.5$; $0 < y \leq 0.9$). Magnetic Susceptibility, Knight Shift, and Longitudinal Relaxation. *Berichte Bunsenges. Für Phys. Chem.* **1988**, *92*, 833–840.
51. Huang, Z.; Zhao, Y.; Hou, H.; Wang, Z.; Mu, Y.; Niu, X.; Han, P. Point Defects Structure and Alloying Effects of V Atoms into Ni3Al Alloy: A First-Principles Study. *Rare Met. Mater. Eng.* **2011**, *40*, 2136–2141.
52. Chong, X.; Hu, M.; Wu, P.; Shan, Q.; Jiang, Y.H.; Li, Z.L.; Feng, J. Tailoring the anisotropic mechanical properties of hexagonal M7X3 (M=Fe, Cr, W, Mo; X=C, B) by multialloying. *Acta Mater.* **2019**, *169*, 193–208. [CrossRef]
53. Zhang, J.-M.; Zhang, Y.; Xu, K.-W.; Ji, V. Young's modulus surface and Poisson's ratio curve for cubic metals. *J. Phys. Chem. Solids* **2007**, *68*, 503–510. [CrossRef]
54. Mao, X.-C.; Liu, K.; Hou, B.-S.; Tan, J.; Zhou, X.-L. Theoretical Investigation of the Structural, Elastic, and Thermodynamic Properties of $MgAl_2O_4$ Spinel under High Pressure. *J. Phys. Soc. Jpn.* **2016**, *85*, 114605. [CrossRef]
55. Chakraborty, A.; Liton, M.N.H.; Sarker, M.S.I.; Rahman, M.M.; Khan, M.K.R. Exploration of the structural, vibrational, electronic, mechanical and thermal properties of $Ru_4Al_3B_2$ and $Ru_9Al_3B_8$: A DFT study. *RSC Adv.* **2023**, *13*, 28912–28930. [CrossRef] [PubMed]
56. Williams, P.D.; Ambaum, M.H.P. *Chapter 4—The Atmosphere Under Gravity, Thermal Physics of the Atmosphere*, 2nd ed.; Elsevier: Amsterdam, The Netherlands, 2021; pp. 65–89.
57. Chen, L.; Wang, Y.; Hao, X.; Zhang, X.; Liu, H. Lightweight refractory high entropy alloy coating by laser cladding on Ti–6Al–4V surface. *Vacuum* **2021**, *183*, 109823. [CrossRef]
58. Rudy, E.; Brukl, C.E.; Windisch, S. CONSTITUTION OF NIOBIUM (COLUMBIUM)-MOLYBDENUM-CARBON ALLOYS. *Trans. Met. Soc. AIME* **1967**, *239*, 1796–1808.
59. Ming, L.C.; Manghnani, M.H.; Katahara, K.W. Phase transformations in the Ti-V system under high pressure up to 25 GPa. *Acta Metall.* **1981**, *29*, 479–485. [CrossRef]
60. Asano, S.; Ishida, S. Electronic structures of Laves phase compounds. *J. Magn. Magn. Mater.* **1987**, *70*, 39–43. [CrossRef]
61. Hagi, T.; Sato, Y.; Yasuda, M.; Tanaka, K. Structure and Phase Diagram of Ti–V–H System at Room Temperature. *Trans. Jpn. Inst. Met.* **1987**, *28*, 198–204.

Disclaimer/Publisher's Note: The statements, opinions and data contained in all publications are solely those of the individual author(s) and contributor(s) and not of MDPI and/or the editor(s). MDPI and/or the editor(s) disclaim responsibility for any injury to people or property resulting from any ideas, methods, instructions or products referred to in the content.